Oxid Met (2014) 81:435–451
DOI 10.1007/s11085-013-9456-1

ORIGINAL PAPER

Transition from Internal to External Oxidation of Mn Steel Alloys

V. A. Lashgari · C. Kwakernaak · W. G. Sloof

Received: 3 September 2013 / Revised: 11 October 2013 / Published online: 25 October 2013

Abstract The transition from internal to external oxidation of Mn-steels depends on temperature, oxygen partial pressure or dew point and alloy composition. A description for this transition includes, besides the diffusion coefficients of Mn and oxygen, also on the critical volume fraction oxide precipitates. This volume fraction for Mn-steel alloys has been determined experimentally and equals 0.2, whereas usually a value of 0.3 is adopted. A low critical volume fraction oxide implies that the alloy is more prone to external oxidation. Oxidation experiments with 1.7, 3.5 and 7.0 wt% Mn-steel alloys at 950 °C, i.e. in the austenitic region, at different oxygen partial pressure or dew points in the range of −45 to +10 °C showed excellent agreement with the oxidation mode predicted using the data obtained for the diffusivities and critical volume fraction oxide.

Keywords Critical volume fraction · Transition · Internal oxidation · Mn steel alloys

Introduction

Prediction of the oxidation mode of an alloy requires not only the knowledge of the inward flux of oxygen (permeability of oxygen) and the outward flux of the selectively oxidizing alloying element, but also the critical volume fraction of the internal oxide precipitates. The transition from internal to external oxidation can take place by blocking of the oxygen diffusion processes upon formation of a critical volume fraction of internal oxide precipitates in the matrix [1]. This critical

V. A. Lashgari · C. Kwakernaak · W. G. Sloof (✉)
Department of Materials Science and Engineering, and Materials Innovation Institute (M2i), Delft University of Technology, Mekelweg 2, 2628 CD Delft, The Netherlands
e-mail: w.g.sloof@tudelft.nl

volume fraction of internal oxides was determined first by Rapp [2] for an Ag–In alloy. The transition occurs when the mole fraction of indium in the alloy exceeds the value of 0.15. Since the molar volume of formed oxide is almost twice the molar volume of matrix, the mole fraction of 0.15 corresponds to the volume fraction of 0.3. The critical volume fraction of internal oxides for transition should be an approximately constant value for a given alloy under any oxidizing conditions, but probably has different values for other systems [2]. However, the value reported for an Ag–In alloy has been used extensively to evaluate the oxidation behavior of a variety of alloys [3–5]. Only deviating values have been reported for the critical volume fraction of internal oxide particles for Ni–Al system [6–8].

Mn is one of the most common alloying elements in steel. Its selective oxidation during annealing prior to galvanizing is of concern, since MnO at the surface reduces the wettability and hence the adhesion with the zinc coating [9]. Therefore, the transition from internal to external oxidation of Mn steel alloys with different Mn content during annealing in the austenitic region was studied. In particular, the critical volume fraction for internal oxidation of Mn in steel was determined. The actual volume fraction of internal oxide precipitates was measured using scanning electron microscopy images of ion-polished cross-sections of internally oxidized samples. For a quantitative assessment of the volume fraction of internal oxide precipitates, backscattered electron images were recorded and converted into binary images thereby discriminating between steel matrix and oxide precipitates. The composition of the oxide precipitates and the matrix in the internal oxidation zone (IOZ) was identified with electron probe X-ray microanalysis (EPMA) and X-ray diffractometry.

The experimental conditions to observe the transition from internal to external oxidation of Mn steel alloys are described. From these experiments the critical volume fraction for the internal oxidation of Mn in steel is determined. Adopting the criterion for the transition from internal to external oxidation [1] an oxidation map is constructed, which displays the internal and external oxidation domains as a function of the Mn concentration and dew point in the annealing atmosphere. The results are compared with experimental data collected from oxidizing steel alloys with 1.7, 3.5 and 7.0 wt% Mn, respectively, at 950 °C and various dew points.

Experimental Procedures

Materials and Sample Preparation

All the samples were prepared from full-hard cold-rolled material with chemical compositions as listed in Table 1. Rectangular coupons with identical dimensions of 20 × 10 mm were cut with a plate cutter from the as-received cold-rolled sheets with a thickness of 0.95 mm. All specimens were grinded with SiC emery paper, starting with P 220 and finishing with P 800.[1] Next, the samples were rinsed with isopropanol and dried in a flow of pure nitrogen. In order to minimize the effect of

[1] The grading system for abrasives is FEPA standard, Federation of European Products of Abrasives.

Table 1 Chemical composition of the steel alloys in weight percent

Alloy	C	Mn	Si	Al	Cr
Fe–1.7 Mn	0.103	1.70	0.049	0.002	–
Fe–3.5 Mn	0.093	3.48	0.053	0.023	0.019
Fe–7.0 Mn	0.084	6.99	0.051	0.029	0.031

surface roughness on the oxidation and producing reproducible surface quality, electrochemical polishing was employed using a Struers LectroPol-5 instrument. The solution for electrochemical polishing was a mixture of 100 ml perchloric acid, 300 ml butanol and 500 ml methanol. The samples were electrochemically polished for 40 s at 20 v and with a flow rate of the electrolyte set at 20 units. Finally, the samples were ultrasonically cleaned in isopropanol, dried in a flow of pure nitrogen and stored in airtight membrane boxes (Agar Scientific, G3319, UK).

Oxidation Experiment

All oxidation experiments were carried out at 950 °C in a horizontal quartz tube furnace (Carbolite MTF 12/38/850, UK) with an inner tube diameter of 30 mm. The temperature in the furnace tube was measured with a NiCr/NiAl (type K) thermocouple at the sample location. The oxidation experiments were carried out for 1, 4, 20 and 30 h, respectively.

A gas mixture of nitrogen (purity: 99.999 vol%) with 5.0 vol% hydrogen (purity: 99.999 vol%) flow of 1,500 ml/min passed the furnace tube at atmospheric pressure. Both gases were filtered separately with the Accosorb (792/40228), Oxysorb (792/52099) and Hydrosorb (792/40226) filters (Messer Griesheim, Germany) for remaining any hydrocarbons, oxygen and moisture, respectively, before admitting to the furnace. The required oxidation condition was realized by addition of evaporated pure water (18.2 MΩ cm at 25 °C) to the gas mixture with a CEM (Controlled Evaporator Mixer: W-101A-120-K, Bronkhorst, The Netherlands). The pure water was de-aerated in a stainless steel container with helium and kept at a pressure of 3 bar. In the first series of experiments, a specified amount of water vapor that was added resulted in a dew point value of +10 °C, which corresponds with an oxygen partial pressure of 2.34×10^{-17} atm. at 950 °C; see Appendix 1. In a second series of experiments, the Mn-steel alloys were oxidized also at 950 °C in a mixture of N_2 + 5 vol% H_2, but with a dew point of −45, −30 and −10 °C. The dew points +10 and −10 °C of the gas mixture were monitored with a cooled mirror analyzer (Optidew, Michell Instruments, UK) within ±0.2 °C. The dew points of −30 and −45 °C were monitored with a solid state sensor (Easidew online, Michell Instruments, UK) within ±2 °C which was calibrated with a cooled mirror analyzer (S4000 TRS, Michell Instrument, UK) within ±0.1 °C. After loading the sample into the cold zone of the quartz furnace tube, the tube was flushed with pure nitrogen for 10 min with 1,000 ml/min. Then, nitrogen gas was switched to the reaction gas, which is composed of nitrogen, hydrogen and water vapor. After reaching the target dew point, the gas mixture was flowing for

additional 5 min to stabilize the conditions. Next, the sample was moved to the hot zone for starting an oxidation experiment. At the end of the experiment, the sample was pulled back immediately to the cold zone and the reaction gas was switched to pure nitrogen. After 10 min of flushing, the sample was taken out of the cold zone under a nitrogen gas flow.

All of the operating parameters, such as: various gas pressures and flows, liquid water amount, gas temperature, furnace temperature, sensor temperature and dew point value, were monitored and controlled continuously via Labview software (version 8.6).

Microstructure and Composition Analysis

X-ray diffraction was used to identify the phases present in the oxidized samples. X-ray diffraction patterns were recorded with a Bruker D8 (Germany) advance diffractometer equipped with a Vantec position sensitive detector and graphite monochromator in the Bragg–Brentano geometry. Data collection was carried out at room temperature using monochromatic Co $K\alpha$ radiation ($\lambda = 0.179026$ nm) in the 2θ region between 30° and 130° with a step size of 0.0426° 2θ and a dwell time of 2 s. The sample with its surface at the Roland circle was placed on a Si {510} substrate and rotated during measurement. Data evaluation was done with the Bruker program EVA.

The surface and cross-section of all oxidized samples were examined with field-emission scanning electron microscope (JEOL, JSM-6500F, Japan) using acceleration voltage of 15 kV. Images were taken using secondary electron and backscattered electron modes. For accurate measurement of particle sizes and distances, the magnification of the microscope was calibrated with a line/grid standard. Furthermore, X-ray microanalysis using electron dispersive spectroscopy was performed (with a Noran System 7, USA) to determine the chemical composition qualitatively. In order to preserve the oxidized samples during cross-section preparation, a high vacuum sputter coater (Leica, EM SCD500, Germany) was employed to deposit a 1 μm Cu layer on the surface. Afterwards, the sample was embedded in an epoxy resin (G2 epoxy resin, Gatan 601.07270, UK). Cross-sections of the oxidized samples were prepared using a cross-section ion-polisher (JEOL, SM-09010, Japan) operating at an accelerating voltage of 3.5 kV and an ion current of 18 μA using the Ar gas (purity: 99.9999 vol%, i.e. 6 N) [10].

The concentration of manganese and oxygen in the IOZ were determined with EPMA. The analysis was performed with a JEOL JXA 8900R (Japan) microprobe using an electron beam with energy of 10 keV and a beam current of 50 nA, employing wavelength dispersive spectrometry. The composition at each analysis location of the sample was determined using the X-ray intensities of the constituent elements after background correction relative to the corresponding intensities of reference materials. The thus obtained intensity ratios were processed with a matrix correction program CITZAF [11]. The points of analysis were handpicked in between the internal oxide precipitates. The stability of the measurement was assessed using a beam location monitor. In case of a small drift of the beam, the measurement was discarded.

The volume fraction of internal oxide precipitates was determined from the secondary electron images of cross sections prepared from the oxidized samples; see above. The images taken in backscattered electron mode were converted into binary images (black and white) and analyzed with image processing software, such as: Adobe Photoshop and/or ImageJ [12]. In the IOZ, the number of black and white pixels was counted. The pixel fractions represent both the area and volume fractions of the matrix and oxide precipitates [13]. Next, the as obtained volume fractions can be transferred into mole fractions considering the relevant molar volumes. The matrix and oxide precipitates are considered to be pure Fe and stoichiometric MnO, respectively. The molar volumes of Fe and MnO are taken equal to 7.10 and 13.21 cm^3/mol, respectively [14].

Since nitrogen gas was used in the oxidizing atmosphere, neither the X-ray diffraction patterns nor the EPMA analysis of the oxidized samples indicated the presence of nitride phases. Moreover, thermodynamic calculations confirmed that no nitrides could be formed in the evaluated steel alloys. Furthermore, presence of water vapor can affect oxidation of alloys. As an example, for alloys forming alumina scales in cyclic oxidation at high temperatures, presence of water vapor decreases the fracture toughness at scale/alloy interface which results in spallation of the scale [15, 16]. However, these phenomena were not observed for studied oxidized samples.

Background

Upon formation of internal oxide particles, diffusion of oxygen within these oxide precipitates is negligible. Hence, diffusion of oxygen takes place through the bulk and along the interface between the oxide particles and the matrix. When the volume fraction of internal oxide precipitates reaches a critical value, i.e. g^*, these internal oxide particles act as the diffusion barriers for oxygen and therefore internal oxidation ceases. Consequently, oxidation proceeds at the alloy surface, which is then called external oxidation. This phenomenon is commonly known as the transition from internal to external oxidation [1, 2].

The volume fraction of internal oxide precipitates can be defined as:

$$g = \frac{N_{BO_v} V_m^{BO_v}}{V_m^{A-B}} \tag{1}$$

where N_{BO_v} represents the mole fraction of BO_v in the IOZ, $V_m^{BO_v}$ and V_m^{A-B} are the molar volume of the oxide and alloy, respectively.

The degree of solute enrichment in the IOZ is defined as [1]:

$$\alpha = \frac{N_{BO_v}}{N_B^{(0)}} = \frac{1}{F(\gamma\varphi^{1/2})}, \tag{2}$$

where $N_B^{(0)}$ is the initial concentration (mole fraction) of the alloying element, $F(u)$ an auxiliary function (with $u = \gamma\varphi^{1/2}$), which reads [17, 18]:

$$F(u) = \sqrt{\pi} u \exp\left(u^2\right) erfc(u) \tag{3}$$

The kinetic parameter γ is resolved from [1, 19]:

$$\frac{N_O^{(s)}}{\nu N_B^{(0)}} = \frac{\exp(\gamma^2) erf(\gamma)}{\varphi^{1/2} \exp(\gamma^2 \varphi) erfc(\gamma \varphi^{1/2})}, \tag{4}$$

where $N_O^{(s)}$ is the mole fraction of oxygen at the external surface (cf. Appendix 2) and ν is the stoichiometry of the concerned oxide. This mole fraction depends on the oxygen partial pressure at the external surface according to the Sievert's law [20]. The oxygen partial pressure may be expressed in terms of dew point for practical reasons, see Appendix 1. The ratio of the diffusion coefficient of the oxygen to the alloying element is expressed as:

$$\varphi = \frac{D_O}{D_B} \tag{5}$$

When considering Eqs. 1 and 2, it is obtained that:

$$N_B^{(0)} = g \frac{V_m^{A-B}}{V_m^{BO_\nu}} F\left(\gamma \varphi^{1/2}\right) \tag{6}$$

When the volume fraction of internal oxide precipitates g (cf. Eq. 1) reaches a critical value, g^*, then the transition from internal to external oxidation takes place. Hence, the critical mole fraction of the alloying element for this transition equals:

$$N_{B\ critical}^{(0)} = g^* \frac{V_m^{A-B}}{V_m^{BO_\nu}} F\left(\gamma \varphi^{1/2}\right) \tag{7}$$

This equation is known as the general criterion for the transition from internal to external oxidation [21].

The critical volume fraction of internal oxide precipitates was determined first by Rapp [2] for Ag–In system and has been used extensively to evaluate the oxidation behaviour of other systems. Here, the g^* value is determined for the binary Mn-steel alloys using the area fraction of internal oxide precipitates.

Results and Discussion

Oxide Precipitation Behavior

For three Mn-steel alloys oxidized at 950 °C with a dew point of 10 °C, the number of internal oxide particles and corresponding mean diameters as a function of oxidation time is shown in Fig. 1. These data were obtained from the backscatter electron images of cross-sections (see Fig. 2) using the method outlined in Appendix 3. The number of internal oxides decreases with oxidation time as a result of coarsening of the oxide precipitates. Furthermore, the mean diameter of the oxide precipitates depends on the initial Mn concentration. For the alloy with a low Mn content (1.7 wt%), the oxidation starts with abundant tiny oxide precipitates; see

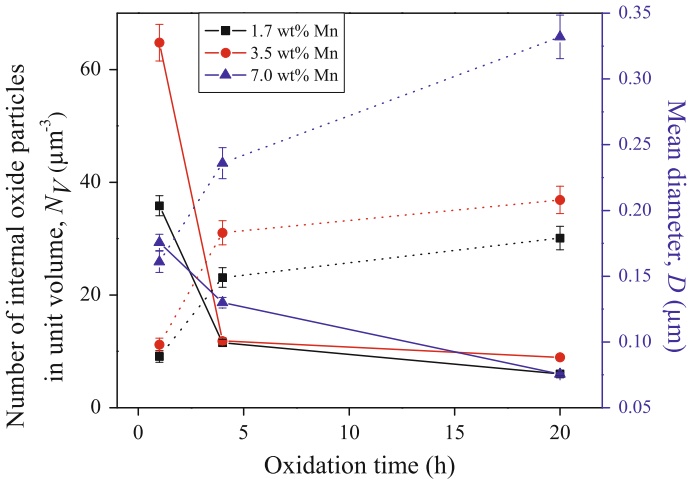

Fig. 1 Number of internal oxide particles per unit volume versus oxidation time for three Mn-steel alloys oxidized at 950 °C in N_2 plus 5 vol% H_2 with a dew point of 10 °C. The mean diameters of internal oxide precipitates are shown as *dashed lines*

Fig. 2a. But for the alloy with a high Mn content (7.0 wt%) less and relatively large internal oxide precipitates are formed; see Fig. 2e.

For diffusion controlled precipitate growth, the number of precipitates per unit volume $Z(X)$ is expressed as [22]:

$$Z(X) = \beta \left(\frac{N_O^{(s)}}{X} \right)^3 \tag{8}$$

$$\text{with } \beta = \left(\frac{1}{N_O^{(s)}} \frac{X}{\Delta X} \right)^3, \tag{9}$$

where X is position of the start of a precipitation and ΔX is the distance between two successive points of nuclei formation (i.e. proceeding of the oxidation front).

Then, the radius of spherical precipitates, when negligible solute enrichment in the IOZ occurs, follows from:

$$Z(X) \frac{4\pi}{3} r^3 = V_{BO_v}^m N_B^{(0)} \tag{10}$$

Hence:

$$r = \left(\frac{3 V_{BO_v}^m N_B^{(0)}}{4\pi\beta} \right)^{1/3} \frac{X}{N_O^{(s)}} \tag{11}$$

$$r \propto \left(N_B^{(0)} \right)^{1/3} \tag{12}$$

Thus, the size of the oxide precipitates increases with the Mn concentration in the steel alloys, as is observed experimentally; see Figs. 1 and 2.

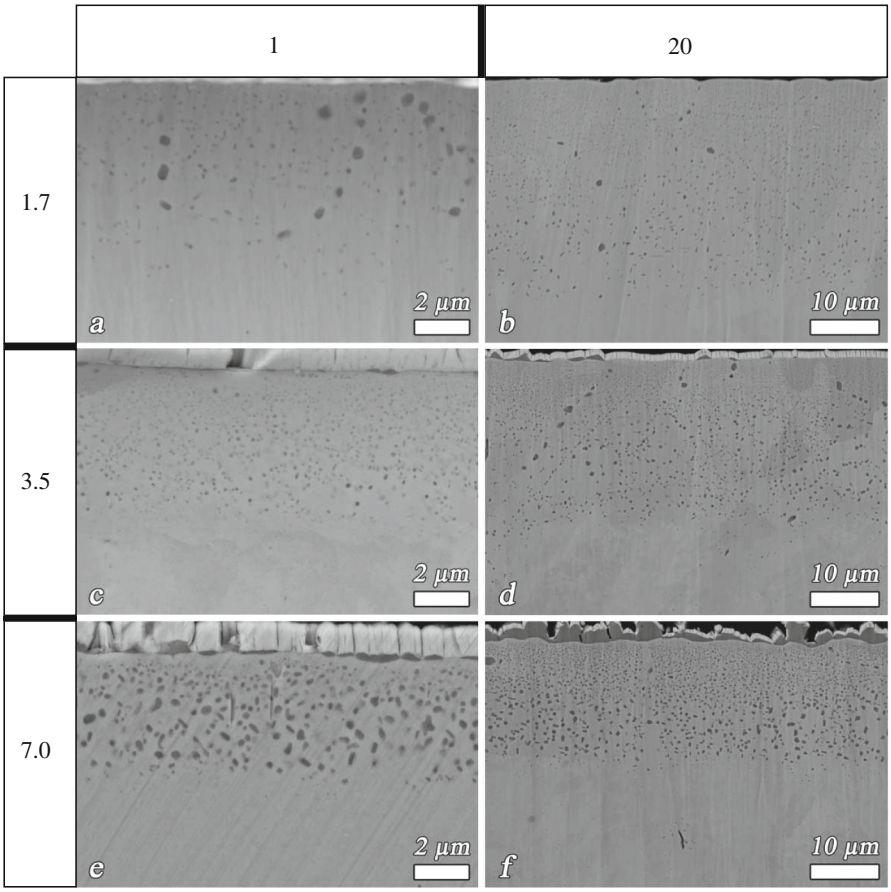

Fig. 2 Backscattered electron images of cross sections of Mn-steel alloys oxidized for 1 and 20 h at 950 °C in N_2 plus 5 vol% H_2 with a dew point of 10 °C. The images in the first and second columns correspond with 1 and 20 h oxidation, respectively. The images in the first, seconds and third rows correspond with the Mn fraction in wt%, respectively. The bright layer on top is a metallic layer applied for sample preparation

The number of internal oxides decreases with oxidation time as a result of coarsening of the oxide precipitates. Furthermore, the mean diameter of the oxide precipitates depends on the initial Mn concentration; see Fig. 1. This implies that an increase of the size of the oxide precipitates is compensated with a decrease of the number of precipitates, which is in accordance with Eq. 10. For a steel alloy with a specific Mn concentration, the number of oxide precipitates decreases with increasing time due to the growth of internal precipitates; see Fig. 1.

Critical Volume Fraction of Internal Oxide Precipitates

Since the steel alloys with different Mn concentrations were oxidized at 950 °C, they were fully transformed into austenite. The high dew point of +10 °C in the gas

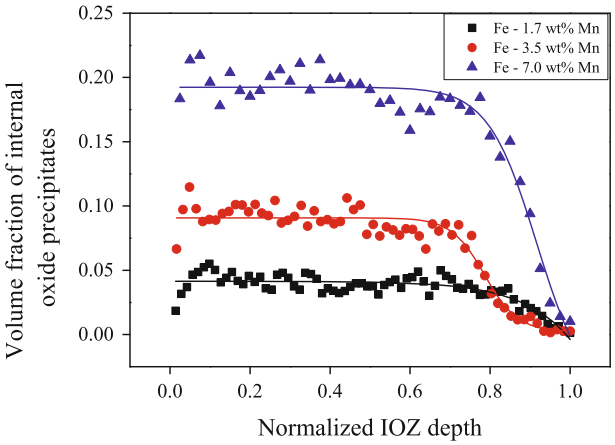

Fig. 3 Volume fraction of internal oxide precipitates versus the normalized depth of IOZ in Mn-steel alloys oxidized for 20 h at 950 °C in N_2 plus 5 vol% H_2 with a dew point of 10 °C

ambient ensured that internal oxidation of MnO was initiated. This dew point, however, is well below that for the formation of FeO (Wüstite), which for the alloys concerned is in the range of 25–75 °C.

The oxide precipitates are clearly visible in the backscatter electron images of cross sections of the oxidized samples; see Fig. 2. The volume fraction of oxide precipitates is virtually constant within the IOZ, but increases with increasing Mn concentration; see Fig. 3. For an oxide with extremely low solubility product, mole fraction of internal oxide precipitates is constant within the IOZ and drops to zero at a sharp boundary. Furthermore, concentration of oxygen beyond the IOZ is zero. In contrast for high solubility product oxide, mole fraction of internal precipitates decreases within the IOZ and oxygen diffuses beyond the oxidation front as well. For Mn oxidation, based on our EPMA measurements, the oxygen concentration is zero beyond the IOZ and volume fraction (corresponding to mole fraction) of internal oxides is almost constant within the IOZ, as can be seen from Fig. 3. Also the volume fraction drops rapidly to zero at the internal oxidation front. Therefore, we considered MnO having a low solubility product albeit not extremely low.

The average volume fraction of internal precipitates was determined for the different Mn steel alloys as a function of oxidation time; see Fig. 4. This volume fraction of internal oxides increases with initial Mn content of the alloy. For the 1.7 wt% Mn alloy, the volume fraction is almost constant with oxidation time. For the 3.5 and 7.0 wt% Mn alloys, however, the volume fraction of internal oxides increases initially with time. Subsequently, the volume fraction of internal oxide precipitates attains a practically constant value.

The initial increase of the volume fraction oxide precipitates observed for the 3.5 and 7.0 wt% Mn alloys and not for the 1.7 wt% Mn alloy may be due to super saturation by Mn of the matrix in the IOZ (N_B^*) which increases with the Mn content of the steel alloy. Then, the concentration of Mn in the matrix of the IOZ is higher than the Mn concentration for MnO in equilibrium as given by the solubility product K_{sp}, hence:

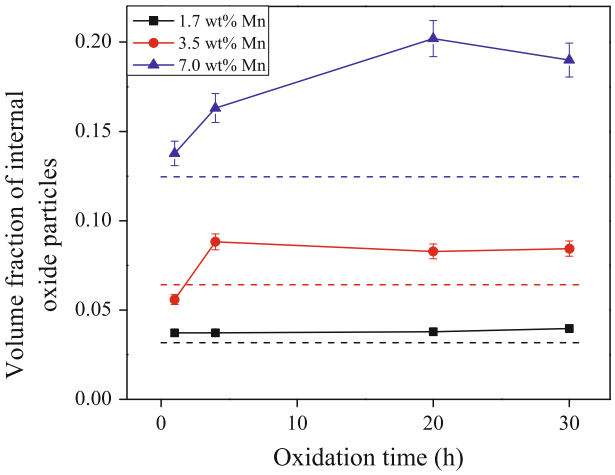

Fig. 4 Volume fraction of internal oxide particles versus oxidation time of Mn-steel alloys oxidized at 950 °C in N_2 plus 5 vol% H_2 with a dew point of 10 °C. The *dotted lines* correspond to the volume fraction of internal oxides if the total amount of Mn in the IOZ was transformed into MnO (i.e. no enrichment and deviating stoichiometry)

$$N^*_{\underline{Mn}} > \frac{K_{sp}}{N^*_{\underline{O}}} \tag{13}$$

$$\text{with}: \; K_{sp} = N_{\underline{Mn}} N_{\underline{O}} \tag{14}$$

Both the solubility product and the concentration of oxygen are constant and the same for all Mn steel alloys, because the temperature (950 °C) and dew point (+10 °C) were kept the same during the oxidation experiments. Thus, the super saturation (see Eq. 13) upon internal oxidation increases with the Mn content of the steel alloy. If complete oxide precipitation in the IOZ does not occur instantaneously, then during subsequent oxidation the remnant Mn in the existing IOZ will be oxidized.

Apparently, instantaneous oxide precipitation occurred only when oxidizing the 1.7 wt% Mn alloy, because the volume fraction of internal oxide particles is constant with time. However, the increase of the volume fraction of oxide with time when oxidizing the 3.5 and 7.0 wt% Mn alloy, suggests that initially super saturation of Mn in the matrix of the IOZ occurred. This is confirmed by X-ray microanalysis of the Mn concentration in the matrix of the IOZ. The Mn concentration in the IOZ for the 1.7 wt% Mn is constant with oxidation time (0.2 wt% Mn), whereas this concentration is initially high for the 7.0 wt% Mn alloys (2.0 wt% Mn after 1 h oxidation), but decreases for longer oxidation times (1.0 wt% Mn after 20 h oxidation). The presence of Mn in the IOZ indicates that MnO is not an extremely low solubility product oxide. However, based on the reasoning above (related to Fig. 3) and zero concentration of oxygen beyond the IOZ, it can be considered as a low solubility product oxide.

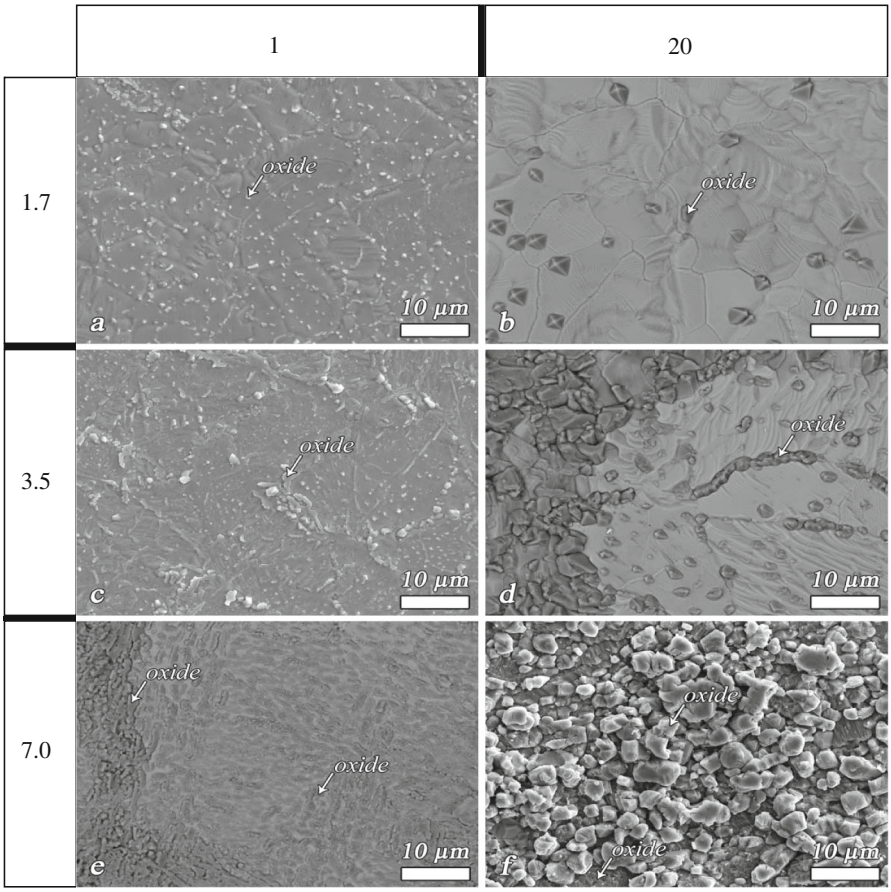

Fig. 5 Secondary and backscattered electron images of surface of the Mn-steel alloys oxidized for 1 and 20 h at 950 °C in N_2 plus 5 vol% H_2 with a dew point of 10 °C. The images in the first and second columns correspond with 1 and 20 h oxidation, respectively. The images in the first, seconds and third rows correspond with the Mn fraction in wt%, respectively

When observing the oxidized surfaces, it can be seen that the surface of the steel with 1.7 wt% Mn alloy consists of unoxidized areas and external oxide particles; see Fig. 5a, b. It is obvious that a transition from internal to external oxidation does not take place even after 20 h oxidation, see Fig. 5b. The only effect of the oxidation time is the increase of size of the iron matrix grains as well as external oxide particles. The coverage with oxides of the surface of the steel with 3.5 wt% Mn alloy increases with oxidation time; see Fig. 5c, d. However, unoxidized areas can be observed still after 20 h of oxidation. The presence of oxide particles on the surface at high dew point (see Fig. 5a, b) is attributed to easy nucleation at surface defects especially along the grain boundaries or any roughness on the surface.

Also the coverage with oxides of the surface of the steel with 7.0 wt% Mn alloy increases with oxidation time; see Fig. 5e, f The whole surface is covered with external oxides after 20 h of oxidation of this alloy indicating the occurrence of the

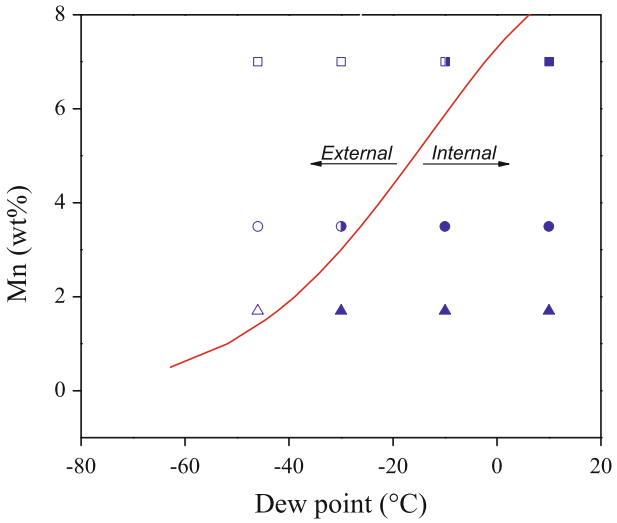

Fig. 6 Oxidation domains for binary Fe–Mn alloys at 950 °C as a function of dew point in a mixture of N_2 plus 5 vol% H_2 using the general criterion, cf. Eq. 7. The line depicting the transition from internal to external oxidation is determined using 0.2 as the critical volume fraction of internal oxides and the diffusion coefficients of oxygen and manganese as obtained from the observed internal oxidation kinetics and Mn concentration depth profiles, respectively. For the molar volume of the oxide the value of stoichiometric MnO [14] was adopted. The *filled, unfilled* and *half-filled symbols* represents: internal, external and simultaneous internal and external oxidation modes, respectively

transition from internal to external oxidation. A closed layer of oxide can be seen in the cross section of the steel alloy with 7.0 wt% Mn oxidized for 20 h; see Fig. 2f.

Clearly, for the 7.0 wt% Mn steel alloy oxidized at 950 °C and dew point of 10 °C the transition from internal to external oxidation occurs. From this result, a value for the critical volume fraction of oxide precipitates g^* can be determined. It follows that for the internal oxidation of Mn in an austenite matrix this critical volume fraction oxide equals 0.20 ± 0.02, which is much less than the generally adopted value of 0.3 [2]. A low value for the critical volume fraction oxide implies that external rather than internal oxidation is promoted. Thus, to oxidize Mn-steel alloys without external MnO formation, a relatively high oxygen partial pressure or dew point is required.

Now, for the Mn steel alloy an oxidation map can be constructed based on Eq. 7 and using Eq. 4, which defines the internal and external oxidation regions, see Fig. 6. This requires the molar volumes of the alloy and oxide as well as the diffusion coefficients of manganese and oxygen in the alloy at 950 °C. The molar volume of the Mn-steels is calculated with ThermoCalc using the TCFE 5 database [23]. The molar volume of MnO is taken 13.21 cm^3/mol [14]. For oxidation at high dew point, which corresponds to higher permeability of oxygen with respect to the alloying element, a simplified relation for the gamma value can be used [1], cf. Eq. 15:

$$\gamma = \left(\frac{N_O^{(s)}}{2\nu N_B^{(0)}} \right)^{1/2} \tag{15}$$

The diffusion coefficient of oxygen was derived from the growth of the IOZ (cf. Eq. 16) using Eq. 15, i.e.:

$$\xi = 2\gamma\sqrt{D_O t}, \tag{16}$$

where ξ is the depth of IOZ and t is time.

Because the presence of internal oxide precipitates accelerates diffusion of oxygen, the values for the diffusion coefficient of oxygen as obtained from Eq. 16 were evaluated as a function of the volume fraction internal oxide precipitates, depicted versus volume fraction of internal precipitates and then extrapolated to zero to exclude effect of oxygen acceleration [24]. The values for the diffusion coefficient of oxygen extrapolated to zero volume fraction oxide precipitates equals 3.35×10^{-7} cm^2/s at 950 °C. This value is of the same order of magnitude as earlier reported for the diffusion coefficient of oxygen in austenite, viz.: 3.53×10^{-7} cm^2/s [25]. The diffusion coefficient of Mn in austenite was derived from the enrichment of Mn as MnO in the IOZ using Eqs. 2–5 and considering the obtained diffusion coefficient of oxygen. The obtained value for the diffusion

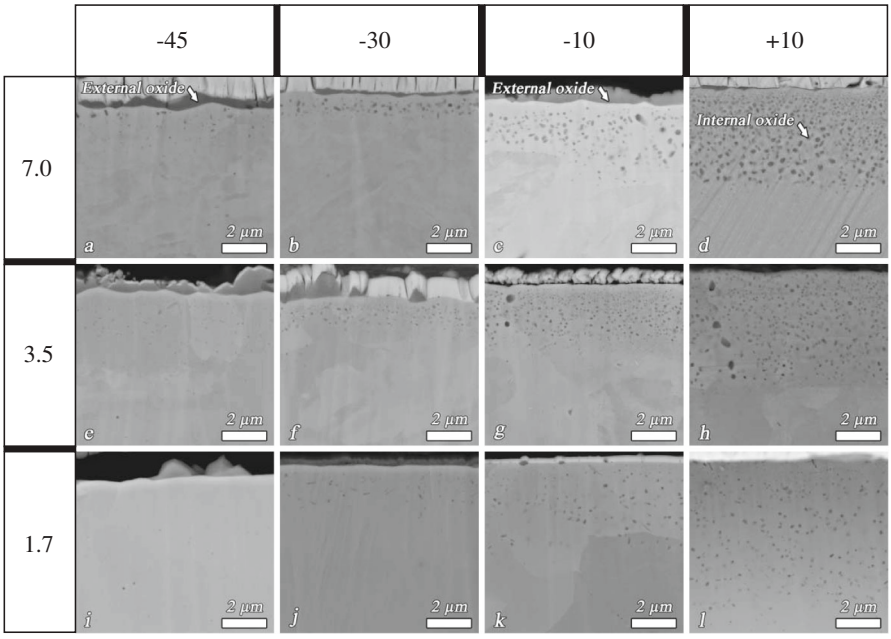

Fig. 7 Backscattered electron images of cross sections of Mn-steel alloys oxidized for 1 (at dew points of 10, −10 and −30 °C) and 4 h (at dew point of −45 °C) at 950 °C in N_2 plus 5 vol% H_2 with various dew points, see Fig. 6 for external versus internal oxidation. The images in the first till the fourth columns correspond with the dew points in °C. The images in the first, seconds and third rows correspond with the Mn fraction in wt%, respectively. The bright layer on top is a metallic layer applied for sample preparation

coefficient of Mn in austenite equals 4.44×10^{-12} cm^2/s at 950 °C, which is in reasonable agreement with earlier reported values for the diffusion coefficient of Mn in austenite, viz.: 1.06×10^{-12} [26] and 9.43×10^{-13} cm^2/s [27].

The oxidation map is displayed in Fig. 6, with the concentration of the oxidizing alloying element and partial pressure of oxygen (expressed as dew point) at the vertical and horizontal axes, respectively. The depicted line in Fig. 6 represents the transition limit between internal and external oxidations. When the initial concentration of the alloying element and partial pressure of the oxygen at the alloy surface are known, the oxidation mode can be predicted. Our observations of the Mn steels oxidized at different dew points (see Fig. 7) are in excellent agreement with the predicted transition between internal and external oxidation mode as depicted in the oxidation map for Mn alloyed steels; see Fig. 6.

Since the critical volume fraction is considered to be a constant, the value for MnO precipitates in austenite can be used to predict the oxidation mode (i.e. internal versus external) as a function of Mn steel alloy composition and temperature.

Conclusions

Upon oxidation of Mn steel alloys in the austenite region and below the oxygen partial pressure or dew point of FeO formation, the oxide consists practically of MnO. In case of internal oxidation, the number of internal oxide precipitates decreases with oxidation time and the mean diameter of these precipitates depends on the initial Mn concentration of the steel alloy.

However, the volume fraction of internal oxide precipitates is practically constant within the IOZ, but increases with Mn concentration of the steel alloy. The volume fraction of internal MnO precipitates may increase with oxidation time depending on the super saturation of Mn in the IOZ, but eventually attains a constant value.

The critical volume fraction of internal MnO precipitates (g^*) in austenite equals 0.2. As confirmed by experimental observations, this critical volume fraction can be used to predict the oxidation mode of Mn-steel alloys annealed within the austenite region.

Acknowledgments This research was carried out under project number MC7.07295a in the framework of the Research Program of the Materials innovation institute (M2i, www.m2i.nl). Financial support from International Zinc Association (IZA, www.zinc.org) is gratefully acknowledged. The authors are indebted to Dr. W. Melfo, Dr. H. Bolt and Dr. M. Zuiderwijk of Tata Steel (IJmuiden, The Netherlands) for valuable discussions and providing the Mn steel alloys. The authors are also grateful to Ing. J. C. Brouwer for all his technical support and assistance with the sample preparation.

Appendix 1

The relation between dew point (DP) and partial pressure of water vapor follows from [28]:

$$\log p_{H_2O} = \frac{9.8DP}{273.8 + DP} - 2.22 \qquad DP \leq 0^{\circ}\mathrm{C} \qquad (1-1)$$

$$\log p_{H_2O} = \frac{7.58DP}{240 + DP} - 2.22 \qquad DP > 0^{\circ}\mathrm{C}, \qquad (1-2)$$

where the units of partial pressure of water vapor (p_{H_2O}) and dew point (DP) are in atmosphere and degree Celsius, respectively. Next, the corresponding partial pressure of oxygen can be calculated with the Gibbs free energy of formation ($\Delta G^0_{H_2O}$) of water vapor [29]:

$$H_{2\,(g)} + \frac{1}{2}O_{2\,(g)} = H_2O_{\,(g)}, \text{ with : } \Delta G^0_{H_2O} = -245519 + 53.35T \text{ (J/mol)}, \quad (1-3)$$

in which T is the absolute temperature in Kelvin.

Appendix 2

For the oxygen solubility in Fe it holds that [25]:

$$\log\left(N_O^{(s)}\right) = \log\left(\frac{p_{H_2O}}{p_{H_2}}\right) - \frac{5000}{T} - 0.67 \qquad \text{bcc} - \text{Fe} \qquad (2-1)$$

$$\log\left(N_O^{(s)}\right) = \log\left(\frac{p_{H_2O}}{p_{H_2}}\right) - \frac{4050}{T} - 1.52 \qquad \text{fcc} - \text{Fe} \qquad (2-2)$$

Here $N_O^{(s)}$denotes the surface concentration of oxygen in mole fraction. p_{H_2O} and p_{H_2} are the partial pressure of water vapor and hydrogen in atm., respectively, and T is the absolute temperature in Kelvin.

Appendix 3

In order to obtain the spatial size distribution of internal oxide precipitates from the area observed in the cross-sections, the Saltykov area method [13] was adopted. This method is based on the relative section areas of the precipitates, i.e. A/A_{max}, where A_{max} is the area of the largest precipitate. When assuming that the precipitates are spherical, then the area A can be related to its diameter D. Next, a series of size groups j is obtained by taking the logarithm of the ratio pertaining to the upper boundary of the subsequent size groups equal to 10^{-1}, i.e. $\log\left(\frac{D_{j+1}}{D_j}\right) = 10^{-1}$

Here, 12 size groups were considered. Next, the number of internal oxide particles divided by the total test area (IOZ) for all of the size groups $(N_A)_i$ was counted (using ImageJ software [12]). These values are substituted in the so-called working equation, which reads [13]:

$$(N_v)_j = \frac{1}{D_j}\left[\begin{array}{l} 1.6461(N_A)_i - 0.4561(N_A)_{i-1} - 0.1162(N_A)_{i-2} - 0.0415(N_A)_{i-3} \\ -0.0173(N_A)_{i-4} - 0.0079(N_A)_{i-5} - 0.0038(N_A)_{i-6} - 0.0018(N_A)_{i-7} \\ -0.0010(N_A)_{i-8} - 0.0003(N_A)_{i-9} - 0.0002(N_A)_{i-10} - 0.0002(N_A)_{i-11} \end{array}\right], \quad (3-1)$$

where $(N_v)_j$ represents the number of particles per unit volume in the j^{th} class interval, where $j \in \{1, 12\}$. The largest particle size corresponds to $j = 1$. For each selected value of j, i is set equal to j, which determines the number of terms used inside the brackets. D_j is the maximum diameter of each size group concerned. The total number of particles per unit volume, N_V, equal the sum of the $(N_v)_j$ values, hence:

$$N_V = \sum_{i}^{j} (N_v)_j \quad (3-2)$$

The mean diameter of the precipitates is obtained from [13], i.e.:

$$\overline{D} = \frac{1}{N_V}\sum_{i}^{j} (N_v)_j D_j \quad (3-3)$$

References

1. C. Wagner, *Zeitschrift für Elektrochemie* **63**, 772 (1959).
2. R. A. Rapp, *Acta Metallurgica* **9**, 730 (1961).
3. F. Gesmundo, Y. Niu, F. Viani and F. C. Rizzo, *Oxidation of Metals* **46**, 441 (1996).
4. Y. Niu, X. J. Zhang, Y. Wu and F. Gesmundo, *Corrosion Science* **48**, 4020 (2006).
5. R. Khondker, A. Mertens and J. R. McDermid, *Materials Science and Engineering A* **463**, 157 (2007).
6. F. S. Pettit, *Transactions of the Metallurgical Society of AIME* **239**, 1296 (1967).
7. J. A. Nesbitt, *Journal of the Electrochemical Society* **136**, 1511 (1989).
8. F. Gesmundo and Y. Niu, *Oxidation of Metals* **50**, 1 (1998).
9. G. M. Song, W. G. Sloof, T. Vystavel and J Th M De Hosson, *Materials Science Forum* **539–543**, 1104 (2007).
10. M. Shibata, *JEOL News* **39**, 28 (2004).
11. J. T. Armstrong, *Quantitative elemental analysis of individual microparticles with electron beam instruments,* in *Electron Probe Quantitation*, K. F. J. Heinrich and D. E. Newbury (Editors), (Plenum Press, 1991), p. 261.
12. *ImageJ*, *image processing and analysis in Java*, available from: http://rsbweb.nih.gov/ij/.
13. A. S. M. Handbook, *Metallography and Microstructures*, vol. 9, (ASM International Materials Park, Newbury, 1992), pp. 124–133.
14. W. M. Haynes (ed.), *CRC Handbook of Chemistry and Physics*, 93rd ed. (Internet version 2013), (CRC Press/Taylor and Francis, Boca Raton, 2012–2013), p. 4.
15. R. Janakiraman, G. H. Meier and F. S. Pettit, *Metallurgical and Materials Transactions A* **30**, 2905 (1999).
16. M. C. Maris-Sida, G. H. Meier and F. S. Pettit, *Metallurgical and Materials Transactions A* **34**, 2609 (2003).
17. C. Wagner, *Journal of the Electrochemical Society* **99**, 369 (1952).
18. J. Crank, *The Mathematics of Diffusion*, (Clarendon Press, Oxford, 1975).
19. R. A. Rapp, *Corrosion* **21**, 382 (1962).

20. D. R. Gaskell, *Introduction to the Thermodynamics of Materials*, 4th ed, (Taylor & Francis, New York, 2003), p. 547.
21. F. Gesmundo and F. Viani, *Oxidation of Metals* **25**, 269 (1986).
22. M. Kahlweit, *Zeitschrift für Physikalische Chemie Neue Folge* **32**, 1 (1962).
23. *Thermo-Calc Software*, available from: http://www.thermocalc.com/.
24. J. Takada, S. Yamamoto, S. Kikuchi and M. Adachi, *Metallurgical Transactions A* **17**, 221 (1986).
25. J. H. Swisher and E. T. Turkdogan, *Transactions of the Metallurgical Society of AIME* **239**, 426 (1967).
26. K. Nohara and K. Hirano, *Transactions of the Iron and Steel Institute of Japan Metals Suppl* **11**, 1267 (1971).
27. H. Oikawa, *Tetsu-To-Hagane* **68**, 1489 (1982).
28. D. Huin, P. Flauder and J.-B. Leblond, *Oxidation of Metals* **64**, 131 (2005).
29. I. Barin, *Thermochemical Data of Pure Substances*, 3rd ed, (VCH, Weinheim, 1995), p. 796.